• Original Paper •

Assessment of Regional Fire Carbon Emissions during 2003–23 Simulated by Multiple CMIP6 Models

Hongzhao WANG[1,2], Jun WANG*[1,2], Junyuan CHEN[1,2], Zishan WANG[1,2], Jiawen ZHU[3], and Qian ZHANG[4]

[1]*International Institute for Earth System Science*, *Nanjing University*, *Nanjing* 210023, *China*

[2]*Jiangsu Provincial Key Laboratory of Geographic Information Science and Technology*, *Key Laboratory for Land Satellite Remote Sensing Applications of Ministry of Natural Resources*, *School of Geography and Ocean Science*, *Nanjing University*, *Nanjing* 210023, *China*

[3]*State Key Laboratory of Earth System Numerical Modeling and Application*, *Institute of Atmospheric Physics*, *Chinese Academy of Sciences*, *Beijing* 100029, *China*

[4]*College of Geodesy and Geomatics*, *Shandong University of Science and Technology*, *Qingdao* 266590, *China*

(Received 26 May 2025; revised 20 November 2025; accepted 12 December 2025)

ABSTRACT

Wildfires play a critical role in the Earth system, affecting climate, carbon cycling, air quality, and human livelihoods. Phase 6 of the Coupled Model Intercomparison Project (CMIP6) provides multi-model simulations of historical and future wildfire carbon emissions, yet substantial uncertainties remain. Here, we evaluate fire carbon emissions from 10 CMIP6 models over 2003–23 using three satellite-based datasets (GFED, GFAS, QFED) across 14 subregions. The multi-model ensemble (MME) largely reproduces the spatial patterns, with a pattern correlation coefficient of 0.64 and normalized standard deviation of 1.00, but overestimates emissions in most regions, particularly the tropics, leading to inflated global totals. Only 5 out of 14 subregions show good agreement with observations. Seasonality is reasonably captured, with most models simulating peak fire months within ±1 month. Sensitivity analysis reveals strong regional variation in fire responses to near-surface air temperature (TAS) and surface soil moisture (SM). The MME correctly identifies TAS as the dominant driver in most high and middle latitudes but misrepresents the relative influence of TAS and SM in key tropical regions. Observationally, widespread declines in tropical fire emissions contribute to an overall global decrease (−0.02 PgC yr^{-2}), but CMIP6 models fail to capture these trends, instead simulating spurious increases that drive unrealistic upward global trends (0.03 PgC yr^{-2}). These discrepancies are largely attributable to inadequate representation of anthropogenic fire suppression and overestimated temperature sensitivity. Our results highlight the need for improved fire-process parameterizations to enhance the reliability of future projections of fire-related carbon emissions under climate change.

Key words: wildfire carbon emissions, CMIP6 models, satellite-based observations, model evaluation, fire–climate sensitivity

Citation: Wang, H. Z., J. Wang, J. Y. Chen, Z. S. Wang, J. W. Zhu, and Q. Zhang, 2026: Assessment of regional fire carbon emissions during 2003–23 simulated by multiple CMIP6 models. *Adv. Atmos. Sci.*, https://doi.org/10.1007/s00376-025-5309-5.

Article Highlights:

- CMIP6 models largely capture spatial fire patterns but overestimate emissions, especially in the tropics, inflating global totals.
- The MME identifies temperature as key in high latitudes but misrepresents temperature–soil moisture roles in the tropics.
- CMIP6 models simulate rising global fire emissions, contradicting observed declines from satellite-based products.

1. Introduction

Wildfires are natural phenomena that significantly impact global ecosystems. They burn approximately 348 million hectares (Mha) annually, accounting for about 3% of the global land surface (Giglio et al., 2013; van der Werf et al., 2017; Archibald et al., 2018). Wildfires affect the terrestrial carbon balance by releasing large quantities of carbon dioxide (CO_2), methane (CH_4), and carbon monoxide (CO) during combustion (Wang et al., 2020; Zheng et al., 2023; Byrne et al., 2024) while altering the carbon dynamics in post-fire vegetation (Flannigan et al., 2009). Every year, wildfires emit around 2.2 Pg of carbon into the atmosphere (van

* Corresponding author: Jun WANG
Email: wangjun@nju.edu.cn

der Werf et al., 2017), highlighting their critical role in the global carbon cycle and their potential impacts on the climate system.

Wildfire activity exhibits strong seasonal cycles and interannual variability, driven by factors such as vegetation productivity, land use changes, and climate extremes (van Marle et al., 2017). In particular, climate change has been shown to intensify fire risk by altering temperature, while increased lightning frequency further amplifies ignition likelihood (Larjavaara et al., 2005; Westerling et al., 2006). Moreover, wildfire dynamics cannot be attributed to climatic conditions or vegetation productivity in isolation; rather, they emerge from the intricate interplay among these and other biophysical factors (Jones et al., 2022). This complexity underscores the need to consider multi-dimensional influences when analyzing fire patterns. Besides, human activities are also particularly influential, as changes in land use, road networks, and population density have been shown to significantly affect fire occurrences (Radeloff et al., 2005; Abatzoglou and Williams, 2016). Thus, human actions play a dual role—both as direct contributors to fire ignitions and as indirect modifiers of fire regimes through land management practices (Martínez et al., 2009).

The interaction between wildfires and climate change is complex and bidirectional. Biogeophysical factors—such as vegetation, topography, and weather conditions—affect fire patterns and the extent of burned areas (Padilla and Vega-García, 2011). For example, soil and weather conditions jointly determine fire ignition likelihood and spread potential (Verdú et al., 2012; He et al., 2021). Warming climates exacerbate wildfire risk by drying fuels and prolonging droughts, as evidenced by the 2019/20 Black Summer bushfires in Southeast Australia, which were fueled by unprecedented heat and dryness (Abram et al., 2021).

Human-induced climate change has become a dominant factor in the increasing frequency and intensity of wildfires over recent decades (Abatzoglou and Williams, 2016). This trend amplifies the already significant impacts of natural climate variability. Fires also feed back into the climate system by releasing greenhouse gases and aerosols, altering atmospheric composition and radiative forcing. These changes influence cloud cover, precipitation patterns, and albedo, creating cascading effects that extend beyond the immediate impact of the fires themselves (Lasslop et al., 2019). Under global warming, more droughts can exacerbate overnight burning, causing more damage to the climate (Luo et al., 2024). This underscores the urgent need to better understand and predict wildfire interactions with the carbon cycle and climate system.

In the past three decades, significant progress has been made in monitoring and modeling wildfires. Early estimates of biomass burning relied on biome-averaged burned area, biomass density, and combustion efficiency values (Seiler and Crutzen, 1980). By the early 2000s, satellite-based burned area products, such as GBA2000 (Grégoire et al., 2003) and GLOBSCAR (Simon et al., 2004), introduced spatially explicit datasets derived from post-fire reflectance. Modern products, such as those based on MODIS data, offer higher resolution and better capture of current global fire activity (Chuvieco et al., 2019; Ramo et al., 2021). However, while these products provide valuable historical insights, they are limited to the satellite observation period, typically beginning in the 1990s (van der Werf et al., 2017).

To address these temporal limitations, Earth system models (ESMs) play a critical role. ESMs simulate interactions among physical, chemical, biological, and anthropogenic processes governing the Earth system (Scholze et al., 2012). Over recent decades, an increasing number of coupled general circulation models (CGCMs) andESMs have begun incorporating fire modules as a critical component to better understand fire–climate interactions (Held et al., 2019; Walters et al., 2019; Zou et al., 2019; Danabasoglu et al., 2020). The Coupled Model Intercomparison Project (CMIP), organized under the World Climate Research Programme (WCRP), has provided standardized platforms for model simulation, projection, evaluation, and comparison for over two decades (Eyring et al., 2016). Now in its sixth phase (CMIP6), CMIP includes improvements over previous iterations and features contributions from dozens of institutions, offering new insights into Earth system dynamics (Eyring et al., 2016). In addition to CMIP, the Fire Model Intercomparison Project (FireMIP) was established to specifically investigate wildfire biogeochemical processes and has substantially advanced global wildfire simulations. Nevertheless, large uncertainties remain in global multi-model estimates of historical (1700–2012) fire carbon emissions (Li et al., 2019), revealing persistent divergence in key processes such as fire occurrence, burned area, and fire-induced carbon fluxes. These limitations highlight the need to further assess wildfire-related processes within the broader CMIP6 modeling framework.

Given the profound effects of wildfires on the Earth system, incorporating fire scenario modeling into ESMs is indispensable (Hantson et al., 2016). Predicting fire regimes under future climate scenarios is critically important, yet the performance of CMIP6 models in simulating fire carbon emissions remains inadequately assessed. To address this gap, we assess fire carbon emission simulations from 10 CMIP6 models equipped with fire modules. Specifically, we (1) compare simulated global spatial patterns against satellite-based products; (2) analyze regional emissions and their seasonal cycles; (3) examine the climate drivers of regional emissions; and (4) evaluate long-term trends. This comprehensive assessment highlights model-data discrepancies and provides insights for improving fire modules in future ESM development.

2. Datasets and methods

2.1. *CMIP6 models*

This study employs fire carbon emissions (variable denoted as "fFire" in CMIP6) alongside two key climate variables—surface soil moisture (variable denoted as "mrsos") and near-surface air temperature (variable denoted as "tas")—from 10 models in CMIP6 (Eyring et al., 2016). These datasets provide global coverage of fire carbon emissions across both historical periods and future scenarios.

The historical simulations (1850–2014) in CMIP6 are primarily driven by observationally based and comprehensive forcing datasets (Eyring et al., 2016). To align with the temporal coverage of the satellite-based products, we extended the historical period to 2023 using outputs from the Shared Socioeconomic Pathways (SSPs). Given the minimal differences in early-year fire emissions among SSP scenarios, SSP2-4.5 was used for the extension. The model outputs are provided as monthly means, with spatial resolutions varying by model. A summary of the models used in this study is presented in Table 1.

Among the 10 models included, fire schemes differ substantially. CMCC-ESM2 employs the Li scheme in CLM4.5, which accounts for natural and anthropogenic ignitions and suppression, as well as agricultural, deforestation, and peat fires (Li et al., 2012, 2013). CESM-WACCM, NorESM2-LM, and NorESM2-MM adopt the updated Li scheme in CLM5, which refines fuel–moisture controls on fire occurrence and spread and removes the dependence of agricultural fires on fuel loading (Li et al., 2012, 2013; Li and Lawrence, 2017). GFDL-ESM4 applies the FINAL scheme in LM4.1, modifying agricultural fire representation to depend solely on cropland and pasture area (Ward et al., 2018).

EC-Earth3-CC, EC-Earth3-Veg, and EC-Earth3-Veg-LR use the GlobFIRM module in LPJ-GUESS, which does not explicitly represent human influences on fire (Thonicke et al., 2001). Because these models provide only annual fire outputs, they were excluded from analyses requiring monthly data. TaiESM1 adopts a modified GlobFIRM version in CLM4 that incorporates human activities (Kloster et al., 2010). MPI-ESM1-2-LR uses a modified SPITFIRE implementation in JSBACH3.2 (Lasslop et al., 2014). Together, these models provide a diverse set of fire parameterizations for evaluating inter-model differences and improving our understanding of fire–carbon–climate interactions.

2.2. *Satellite-based global fire carbon emission products*

We used multiple satellite-based global fire carbon emission datasets to evaluate the fire carbon emissions simulated by CMIP6 models. Specifically, we employed the Global Fire Emissions Database version 4 (GFED4s; van der Werf et al., 2017), the Global Fire Assimilation System version 1.2 (GFASv1.2; Kaiser et al., 2012), and the Quick Fire Emissions Datasets version 2.6 (QFEDv2.6; Koster et al., 2015).

GFED4s provides global estimates of carbon emissions from biomass burning, capturing both large-scale and small-scale fires. Emissions are estimated by combining the MODIS burned-area product with fuel consumption per unit area. The fuel consumption is derived from the product of fuel load and combustion completeness. The dataset offers spatial and temporal insights into global fire activity at a horizontal resolution of 0.25° × 0.25°, available from 1997 onward (Giglio et al., 2013).

GFASv1.2 utilizes satellite-observed fire radiative power (FRP) to generate high-resolution, near-real-time estimates of biomass burning emissions. The FRP observations assimilated into the system are from the MODIS instruments aboard NASA's Terra and Aqua satellites. Emission estimates are calculated by multiplying the FRP by biome-specific conversion factors. Through the assimilation of these FRP observations, GFASv1.2 provides daily emission estimates of key

Table 1. Summary of the CMIP6 models used in this study.

Institute	Model	Resolution (lon. × lat.)	Fire scheme	Reference
NCAR	CESM2-WACCM	1.25° × 0.9375°	Li (Li et al., 2012, 2013; Li and Lawrence, 2017)	Danabasoglu (2019)
CMCC	CMCC-ESM2	1.25° × 0.9375°	Li (Li et al., 2012, 2013)	Lovato et al. (2021)
EC-Earth-Consortium	EC-Earth3-CC	0.7° × 0.7°	GlobFIRM (Thonicke et al., 2001)	EC-Earth Consortium (2020a)
EC-Earth-Consortium	EC-Earth3-Veg	0.7° × 0.7°	GlobFIRM (Thonicke et al., 2001)	EC-Earth Consortium (2019)
EC-Earth-Consortium	EC-Earth3-Veg-LR	1.125° × 1.125°	GlobFIRM (Thonicke et al., 2001)	EC-Earth Consortium (2020b)
NOAA-GFDL	GFDL-ESM4	1.25° × 1°	FINAL (modified from Li) (Ward et al., 2018)	Krasting et al. (2018)
MPI-M	MPI-ESM1-2-LR	1.875° × 1.875°	modified SPITFIRE (Lasslop et al., 2014)	Wieners et al. (2019)
NCC	NorESM2-LM	2.5° × 1.875°	Li (Li et al., 2012, 2013; Li and Lawrence, 2017)	Seland et al. (2019)
NCC	NorESM2-MM	1.25° × 0.9375°	Li (Li et al., 2012, 2013; Li and Lawrence, 2017)	Bentsen et al. (2019)
AS-RCEC	TaiESM1	1.25° × 0.9375°	Modified GlobFIRM (Kloster et al., 2010)	Lee and Liang (2023)

atmospheric constituents, including CO_2, CO, CH_4, aerosols, and various trace gases. Covering the period from 2003 to the present at a spatial resolution of 0.1° × 0.1°, GFASv1.2 serves as a valuable dataset for atmospheric composition studies, climate modeling, and air quality forecasting.

QFEDv2.6 was developed for integration into NASA's Goddard Earth Observing System (GEOS) modeling and data assimilation frameworks. The system computes emissions by gridding FRP observations from the MODIS instruments aboard the Terra and Aqua satellites and then applying species-specific emission coefficients. It provides daily mean emissions of a wide range of atmospheric constituents—including black carbon, organic carbon, sulfur dioxide (SO_2), CO, CO_2, and $PM_{2.5}$—at a spatial resolution of 0.1° × 0.1° from 2000 to 2025.

To ensure consistency with the model outputs, this study focuses on CO_2 among the various atmospheric constituent emissions provided in the satellite-based products.

2.3. *Climate datasets*

Surface soil moisture (SM) and near-surface air temperature (TAS) were obtained from the ERA5-Land dataset (Muñoz-Sabater et al., 2021), a high-resolution climate reanalysis product developed by the European Centre for Medium-Range Weather Forecasts (ECMWF). ERA5-Land is generated by rerunning the land component of the ECMWF model, offering improved spatial detail over the standard ERA5 reanalysis for land surface variables. It has a spatial resolution of 0.1° × 0.1° and spans the period from 1950 to the present, making it well suited for studies in agriculture, hydrology, and land–atmosphere interactions.

2.4. *Subregions*

To assess model performance across different geographical areas, we adopted the GFED partitioning, which divides the globe into 14 distinct regions (Fig. 1). This standardized framework has been widely used in previous research (Giglio et al., 2010, 2013; Andela et al., 2019; Liu et al., 2022; Gallo et al., 2023) to facilitate comparisons of fire emissions and model outputs. By accounting for regional differences in climate, vegetation, and fire regimes, the GFED partitioning effectively captures the spatial heterogeneity of fire activity and its influence on carbon emissions.

2.5. *Statistical methods*

We applied a suite of statistical methods to analyze and evaluate fire carbon emissions for the selected CMIP6 models. To ensure spatial consistency and enable direct comparison with reference datasets, all model outputs and satellite-based products were resampled to a uniform spatial resolution of 1° × 1° using a first-order conservative remapping approach (Jones, 1999). This approach minimizes biases arising from differences in native spatial resolutions across datasets. Our analysis focuses on the period 2003–23, aligning with the temporal coverage of satellite-based products to ensure a robust model evaluation.

To quantitatively assess model performance, we employed statistical metrics featured in the Taylor Diagram framework (Taylor, 2001), including the pattern correlation coefficient (r), centered root-mean-square error (RMSE), and standard deviation. The Taylor Diagram facilitates a concise and informative comparison between individual model output and reference products (Gleckler et al., 2008).

Given the strong influence of climate conditions on

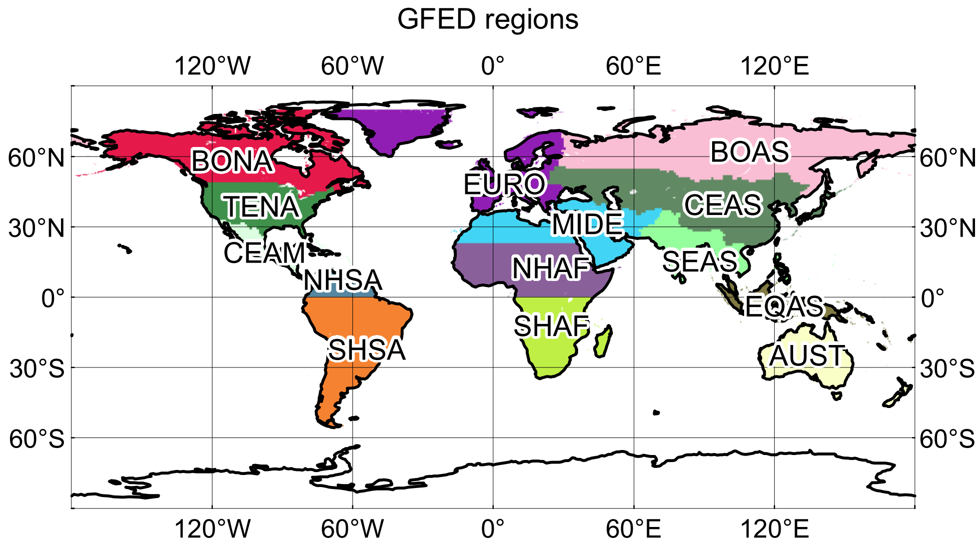

Fig. 1. The 14 regions defined by the Global Fire Emissions Database (GFED) used in this study. The regional abbreviations are: BONA (Boreal North America), TENA (Temperate North America), CEAM (Central America), NHSA (Northern Hemisphere South America), SHSA (Southern Hemisphere South America), EURO (Europe), MIDE (Middle East), NHAF (Northern Hemisphere Africa), SHAF (Southern Hemisphere Africa), BOAS (Boreal Asia), CEAS (Central Asia), SEAS (Southeast Asia), EQAS (Equatorial Asia), and AUST (Australia and New Zealand).

wildfire activity (Jones et al., 2022), we also evaluated the models' ability to capture the relationship between fire emissions and climate variables. Sensitivity analyses were conducted using SM and TAS as predictors. Since most fire emission data are at relatively low levels and only a few extreme fire events produce very high emissions, the data exhibit a highly positive skewed distribution. Therefore, we applied a logarithmic transformation to the data before performing linear regression for sensitivity analysis. Sensitivity was quantified via the following standardized regression model:

$$\log(\text{fFire})_{\text{standardized}} = \alpha + \beta x_{\text{standardized}},$$

where fFire represents monthly fire carbon emissions above the 90th percentile (excluding low emissions), and $x_{\text{standardized}}$ denotes either standardized SM or TAS. Here, α denotes the baseline log-transformed fire carbon emissions when the standardized predictor is zero. The coefficient β quantifies the sensitivity of fire carbon emissions to SM or TAS. Standardization allows for direct comparison of sensitivity magnitudes across variables.

Additionally, we examined long-term trends in fire carbon emissions using both model outputs and satellite-based products. By integrating these statistical methods, we provide a comprehensive evaluation of the models' capabilities and limitations in simulating fire emissions.

3. Results

3.1. *Global and regional carbon fluxes induced by wildfires*

We evaluated the spatial distribution of global fire emissions simulated by CMIP6 models by comparing the multi-model ensemble mean (MME) with satellite-based products over the period 2003–23 (Fig. 2). Satellite-based products show that the highest fire carbon emissions occur in the tropics, particularly in the semi-arid regions flanking the equator in Africa (Fig. 2a). Emissions are also evident at mid-to-high latitudes, notably in Canada and eastern Siberia near 60°N, though with lower intensities compared to tropical regions. The zonal distribution of satellite-based fire emissions exhibits a bimodal structure in the tropics, with peaks around 10°N and 10°S. The Southern Hemisphere peak is slightly stronger, largely due to combined contributions from South America and Africa. A weaker emission peak is also observed near 60°N, associated with boreal fires.

Overall, the MME successfully reproduces the general spatial pattern of fire carbon emissions, including the predominance of tropical emissions over those at higher latitudes (Fig. 2b). This performance can be partly attributed to the CMIP6 models' reasonable ability to reproduce the spatial patterns of key environmental drivers, such as temperature and soil moisture, in agreement with observations (Figs. S1 and S2 in the electronic supplementary material). However, notable biases remain in the simulated magnitude of emissions across many regions. The MME overestimates emissions in South America—particularly in the Amazon—as well as in the African rainforest and the Indo-China peninsula. Conversely, it underestimates emissions in the semi-arid regions of Africa, northern Australia, and the high latitudes of eastern Siberia (Fig. 2c). The bimodal tropical structure is less pronounced in the MME compared to observations. The anomalously strong emissions near 10°S are primarily driven by exaggerated emissions in South America, which are nearly as strong as those in the southern equatorial region of Africa (Fig. 2b). Discrepancies over the Amazon and equatorial African rainforests result in the largest simulation biases near the equator (Fig. 2c). Most individual models reproduce spatial patterns broadly consistent with observations. However, some models—such as CESM2-WACCM, CMCC-ESM2, and members of the NorESM2 family—exhibit pronounced biases in simulating emissions at high northern latitudes. The spatial patterns simulated by each individual model are shown in Fig. S3 in the electronic supplementary material.

Quantitatively, we employed the Taylor Diagram to assess the agreement between model simulations and satellite-based observational products (Fig. 3). The spatial correlation coefficient between the MME and the observations is 0.64, with a normalized standard deviation of 1.00 and a centered root-mean-square (RMS) difference of 0.85. Individual models exhibit spatial correlation coefficients ranging from 0.32 (CMCC-ESM2) to 0.60 (EC-Earth3-Veg), indicating that most models are able to broadly capture the observed spatial pattern of fire carbon emissions. However, the standard deviations among models vary substantially, ranging from 0.76 (TaiESM1) to 2.00 (CESM2-WACCM), with most models showing higher-than-observed spatial variability. The centered RMS differences, which reflect the magnitude of spatial mismatches in fire emission distributions, range from 0.96 (TaiESM1) to 1.77 (CESM2-WACCM).

Figure 4 shows the total fire carbon emissions across the 14 GFED regions from 2003 to 2023. Comparisons indicate that the MME falls within the observational range in only 5 of the 14 regions—specifically, BONA, NHAF, SHAF, EQAS, and AUST (Fig. 4). In contrast, fire carbon emissions are underestimated by the MME only in BOAS. In the remaining eight regions, the MME systematically overestimates emissions. Notably, the overestimation is particularly evident in tropical regions (30°S–30°N), which contributes substantially to the overall global overestimation of fire carbon emissions.

Although the MME in BONA, NHAF, SHAF, EQAS, and AUST align with the observational range for each region, substantial inter-model variability exists. In BONA, only four models—the three EC-Earth3 variants and TaiESM1—produce estimates within the observational range. The remaining models either overestimate emissions (e.g., CMCC-ESM2, GFDL-ESM4, MPI-ESM1-2-LR) or underestimate them (e.g., CESM2-WACCM, both NorESM2 variants). In NHAF, only GFDL-ESM4 aligns with observations, while all EC-Earth3 models overesti-

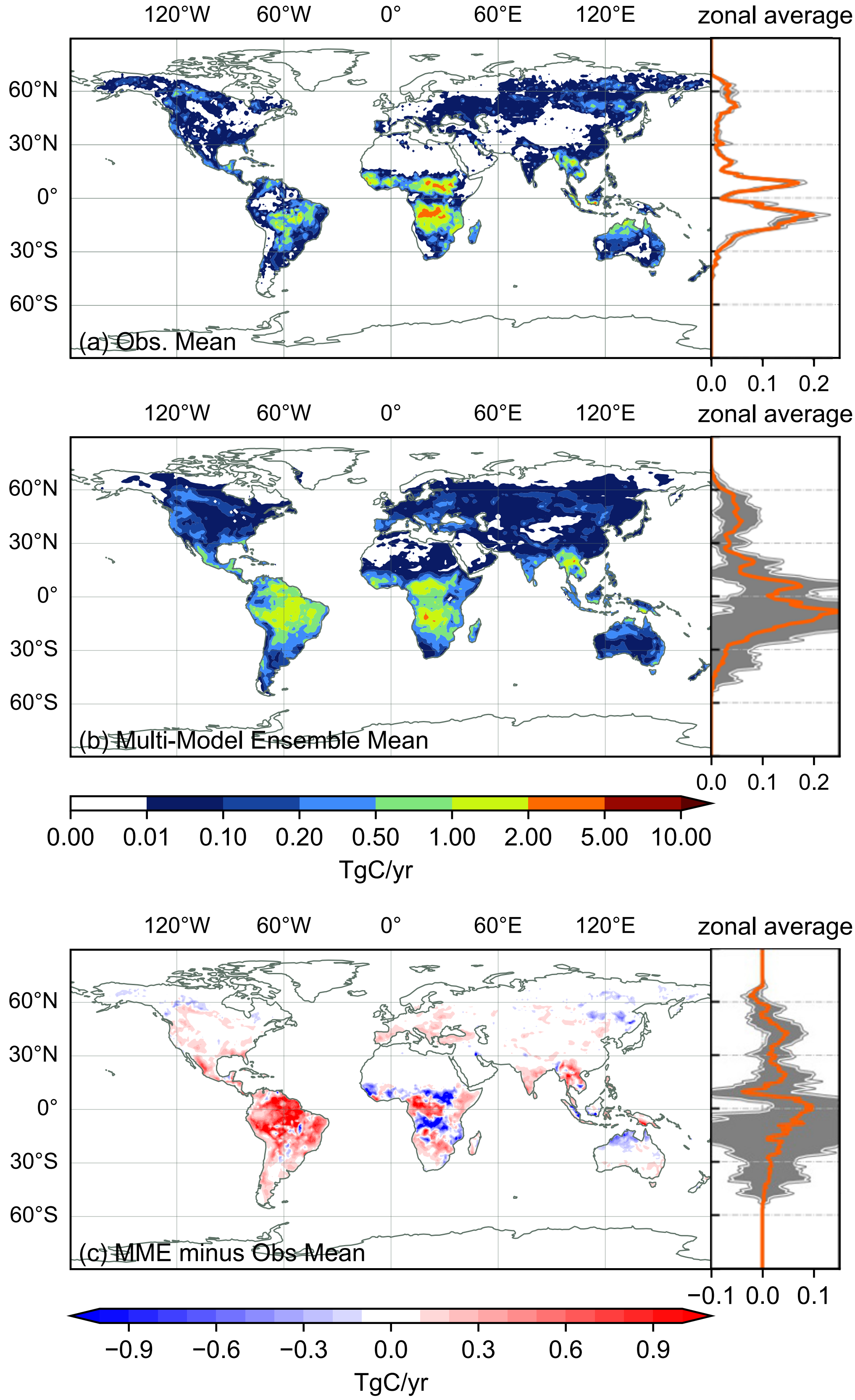

Fig. 2. Global patterns of multi-year average fire carbon emissions during 2003–23 from (a) the observation ensemble, (b) the CMIP6 MME, and (c) the MME bias relative to the observation ensemble. Line plots to the right of each figure show the corresponding zonal average values; shaded areas indicate the range across models in the MME and the observation ensemble.

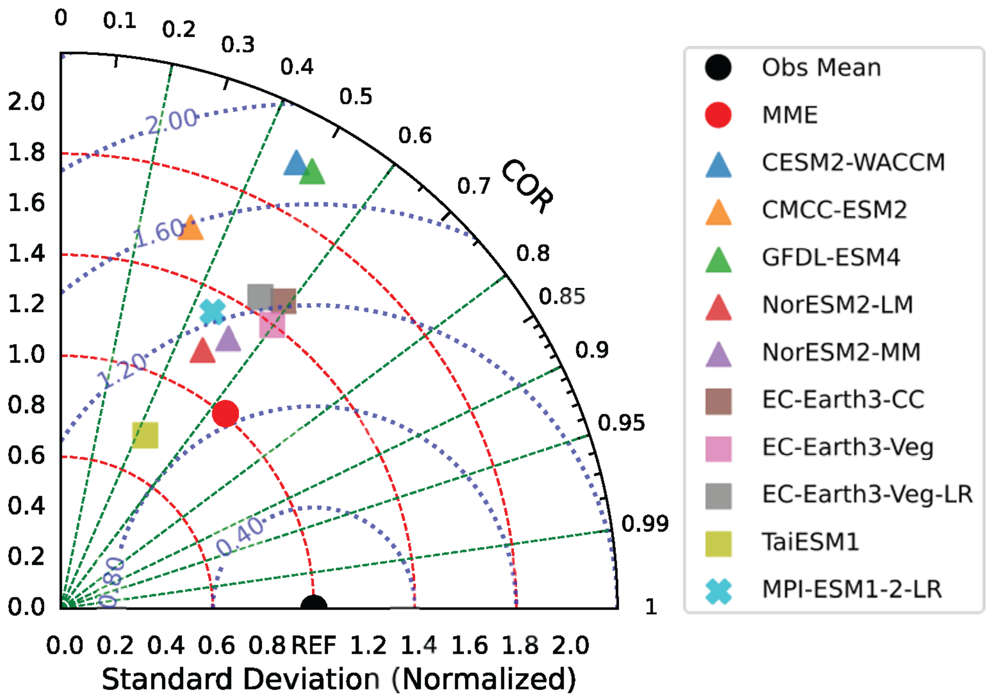

Fig. 3. Taylor Diagram of fire carbon emissions in individual CMIP6 models relative to the ensemble of satellite-based observational products. Triangles represent models employing the Li scheme and its modified version; squares denote models using the GlobFIRM scheme and its modified version; and crosses indicate models implementing the modified SPITFIRE scheme. The red dashed arcs represent normalized standard deviations; the green dashed lines represent pattern correlation coefficients; and the blue dashed contours show centered root-mean-square (RMS) differences. The reference point for the observations is located at a normalized standard deviation of 1.0 and a correlation coefficient of 1.0.

mate, and the rest (CESM2-WACCM, CMCC-ESM2, MPI-ESM1-2-LR, NorESM2 variants, TaiESM1) underestimate emissions. In SHAF, four models (CESM2-WACCM, EC-Earth3-Veg-LR, MPI-ESM1-2-LR, NorESM2-MM) fall within the observational range. Three models (EC-Earth3-CC, EC-Earth3-Veg, GFDL-ESM4) overestimate, while another three (CMCC-ESM2, NorESM2-LM, TaiESM1) underestimate emissions. In EQAS, most models fall within the observational range, except CMCC-ESM2, which overestimates, and MPI-ESM1-2-LR, which underestimates emissions. In AUST, six models are within the range, while four (CMCC-ESM2, MPI-ESM1-2-LR, NorESM2-LM, TaiESM1) overestimate.

In regions where the MME overestimates emissions—such as CEAM, NHSA, SHSA, EURO, CEAS, and SEAS—most individual models also overestimate, except a few exceptions (e.g., MPI-ESM1-2-LR and GFDL-ESM4). In BOAS, where the MME underestimates emissions, only GFDL-ESM4 and MPI-ESM1-2-LR match observations, while all other models underestimate.

In the tropics, most models overestimate fire carbon emissions, except for TaiESM1 (which falls within the range) and two models (CMCC-ESM2 and MPI-ESM1-2-LR) that underestimate. At the global scale, eight models overestimate total emissions, while only CMCC-ESM2 and TaiESM1 deviate from this general pattern.

3.2. *Seasonal cycle*

We find that, although the magnitudes of fire carbon emissions differ somewhat among the three satellite-based products, they exhibit consistent seasonal patterns and peak timings across the GFED regions. In comparison, most CMIP6 models are able to broadly capture the timing of the fire season (Fig. 5). Even when deviations occur, the simulated peak fire emissions typically differ from the observed peaks by no more than one month. However, several region-specific issues remain. In the BOAS region, none of the models effectively capture the spring fires, resulting in a failure of the MME to represent emissions from April to May. In the EURO, TENA, and CEAS regions, the models produce pronounced spurious fire carbon emissions during boreal summer, while observations show weak seasonal variability. In NHSA, although the MME reproduces the February–April peak, it erroneously simulates a secondary peak from September to November. Overall, the MME struggles to accurately represent fire seasonality in temperate North America and the mid- to-high latitude regions of Asia. These seasonal mismatches lead to substantial deviations between simulated and observed fire-season emissions, contributing to the overestimation of annual fire carbon emissions in most regions

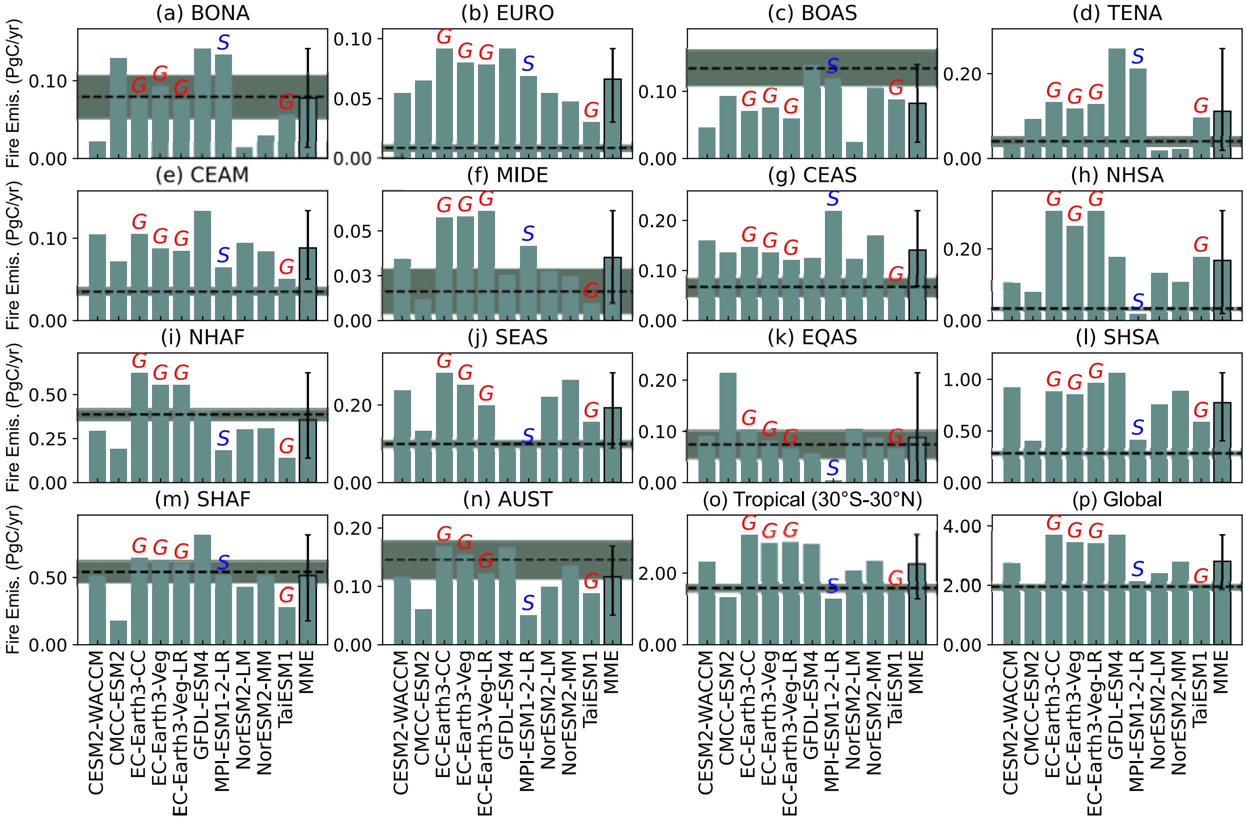

Fig. 4. Total fire carbon emissions from 2003 to 2023 across GFED regions, tropical regions (30°S–30°N), and the global total. The dashed line represents the ensemble mean of the three satellite-based products, with the shaded area indicating one standard deviation. Red "G" labels identify models employing the GlobFIRM scheme and its modified versions; blue "S" labels denote models using modified SPITFIRE schemes; and unlabeled bars represent models based on the Li scheme and its variants. The bars represent fire carbon emissions simulated by individual CMIP6 models while the Multi-Model Ensemble (MME) is indicated with a black border. Error bars denote the inter-model spread.

(8 out of 14), as shown in Fig. 4.

3.3. *Sensitivities to temperature and soil moisture*

Fire activity is jointly influenced by atmospheric conditions and fuel availability, with TAS and SM serving as two primary controlling environmental factors (Flannigan et al., 2009; Sommers et al., 2014; Jones et al., 2022). To assess the sensitivity of fire carbon emissions to these variables, we performed a standardized sensitivity analysis across different regions (Fig. 6). The resulting scatter plots reveal regionally distinct patterns in model sensitivity to SM and TAS.

In high-latitude Northern Hemisphere regions (BONA, EURO, BOAS; Figs. 6a–c), the MME sensitivity to TAS closely agrees with the observational ensemble, except in EURO where it is slightly overestimated. Inter-model spread in TAS sensitivity is relatively low, with only a few models deviating notably. Simultaneously, the MME sensitivity to SM is consistent with observations in BONA and EURO but exhibits exaggerated sensitivities in BOAS, which is also reflected across most individual models.

In midlatitude regions (primarily TENA, CEAM, MIDE, and CEAS; Figs. 6d–g), the MME generally exhibits stronger sensitivity to both TAS and SM than observed, particularly in TENA and CEAS. Most models follow this trend. In CEAM and MIDE (Figs. 6e, f), the sensitivity to SM is notably stronger than observed, while TAS sensitivity remains close to the observational estimates.

In tropical and Southern Hemisphere extratropical regions (NHSA, NHAF, SEAS, EQAS, SHSA, SHAF, and AUST; Figs. 6h–n), the MME's TAS sensitivity broadly aligns with observations in NHSA and NHAF. However, in SEAS and EQAS, the MME exhibits opposite temperature responses compared to the observations—positive sensitivity in SEAS and negative in EQAS—while other regions show overestimated TAS sensitivity. Regarding SM, the MME aligns well with observations in NHSA, NHAF and SHSA, but underestimates sensitivity in SHAF, EQAS, and AUST. Notably, SEAS is the only region where the MME overestimates SM sensitivity. Across all regions, individual models exhibit considerable variability in both TAS and SM sensitivities, highlighting substantial inter-model uncertainty.

We assessed the relative importance of SM and TAS in influencing fire carbon emissions across the 14 GFED regions for each CMIP6 model (Fig. 7). Satellite-based products suggest that in five mid-to-high latitude regions—BONA, EURO, BOAS, MIDE and CEAS—fire emissions are primarily influenced by TAS, while SM is the dominant driver in the remaining regions. The MME correctly identifies

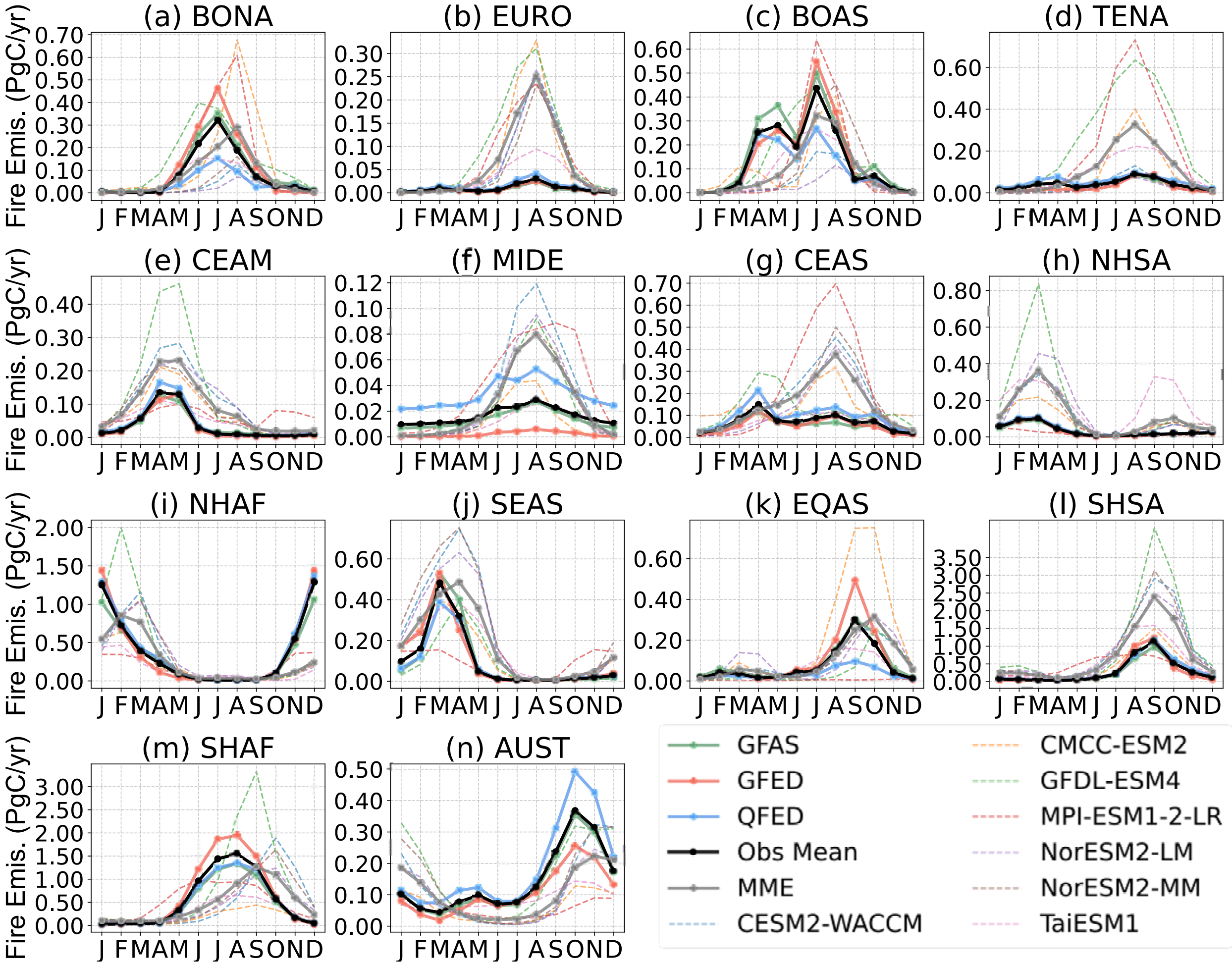

Fig. 5. Seasonal cycle of fire carbon emissions averaged from 2003 to 2023 across the 14 GFED regions, comparing CMIP6 model outputs and observational data. Black solid lines represent the average of three satellite-based products, while the gray solid lines indicate the MME. The EC-Earth3 series models are excluded due to the lack of monthly data availability, as only yearly data are provided.

TAS as the more influential factor in these TAS-dominated regions. In contrast, the MME incorrectly attributes greater importance to TAS in three tropical and southern extratropical regions—TENA, SHSA and AUST—where satellite-based data indicate SM as the primary driver. While individual models generally align with the MME in many regions, notable inconsistencies exist. For instance, in SEAS, most models incorrectly identify TAS as dominant, but the MME correctly suggests SM dominance.

In regions with high fire activity—BOAS, NHSA, NHAF, EQAS, SHSA, SHAF, AUST—only SHSA and AUST show complete disagreement between observations, the MME, and individual models regarding the dominant factor. In other high-activity regions, most models are able to replicate the observed controlling variable.

3.4. *Trends*

The frequency and intensity of wildfires have undergone substantial changes under global warming. Here, we quantitatively assessed trends in annual fire carbon emissions during 2003–23 based on satellite-derived products and the CMIP6 MME across 14 regions, the tropics, and the globe (Fig. 8). Observationally, regional trends fall into three categories:

(1) A significant increase in emissions over BONA and MIDE;

(2) A significant decrease over SHSA, NHAF, SHAF, CEAS, and SEAS, mostly in tropical regions, contributing almost entirely to the declining trend in total tropical emissions (−0.0246 PgC yr^{-2}, Fig. 8o), and hence the global decrease;

(3) No significant trend in the remaining regions.

In comparison, the CMIP6 MME captures the significant increase over BONA (0.0016 PgC yr^{-2}, $p < 0.05$; Fig. 8a) but fails to reproduce the rising trend in MIDE, where it simulates no significant change (Fig. 8f). Notably, the MME does not reproduce the observed declines in tropical regions; instead, it shows insignificant trends across most of these regions, with the exception of a significant increase over SHSA (0.0177 PgC yr^{-2}, $p < 0.05$; Fig. 8l). Alongside a significant increase in NHSA (0.0061 PgC yr^{-2}, $p < 0.05$; Fig. 8h)—a region with no observed trend—these biases lead to an overall significant increase in tropical fire emissions

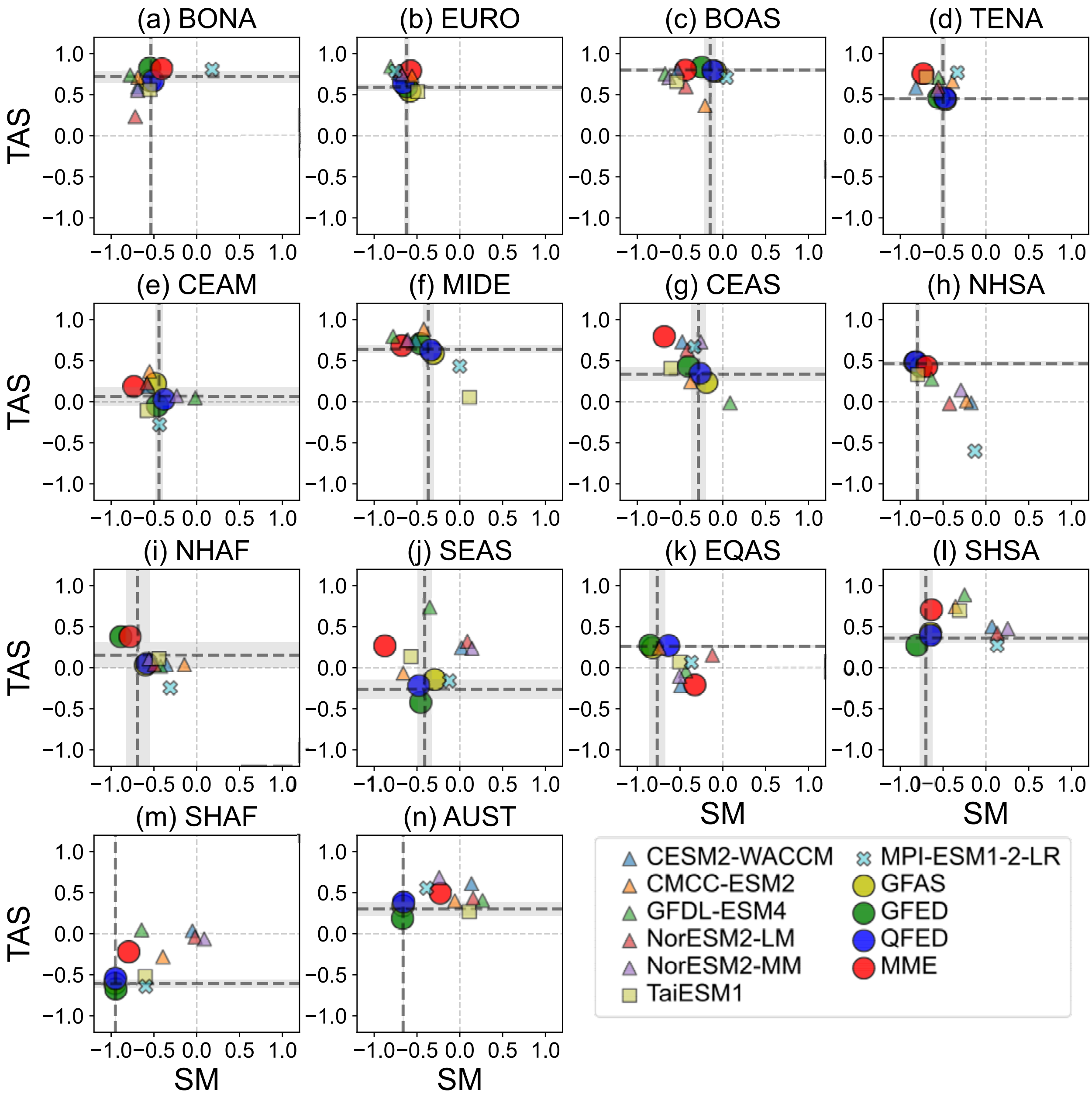

Fig. 6. Scatter plots of the standardized sensitivity of fire carbon emissions to surface soil moisture (SM) and near-surface air temperature (TAS). Triangles represent models employing the Li scheme and its modified version; squares denote models using the GlobFIRM scheme and its modified version; and crosses indicate models implementing the modified SPITFIRE scheme. The thick gray dashed lines represent the multi-product mean deviated from three satellite-based datasets, with the shaded area indicating one standard deviation.

in the MME (0.0269 PgC yr^{-2}, p < 0.05; Fig. 8o). For regions with no significant trends in the observations, the MME generally reproduces these patterns, except in TENA and NHSA. In summary, the overestimation of tropical fire emissions in the MME almost entirely explains the model-derived global increase in fire carbon emissions during 2003–23 (Fig. 8p).

The global spatial patterns of fire carbon emission trends (Fig. 9) show that all satellite-based products and their ensemble mean consistently indicate significant declines over the semi-arid regions straddling the equator in Africa, the southeastern Amazon, and Southeast Asia (Figs. 9a–d)—areas with historically high fire emissions (Fig. 2a). These decreases can partially be attributed to enhanced human fire suppression (Andela et al., 2017).

In contrast, most individual CMIP6 models fail to reproduce these declining trends, particularly over equatorial Africa and the southeastern Amazon, likely due to their limited representation of anthropogenic suppression. Instead, they tend to overestimate emissions in tropical rainforests, including central Africa, the Amazon, and Southeast Asia. Notably, the overestimated increase in fire emissions over

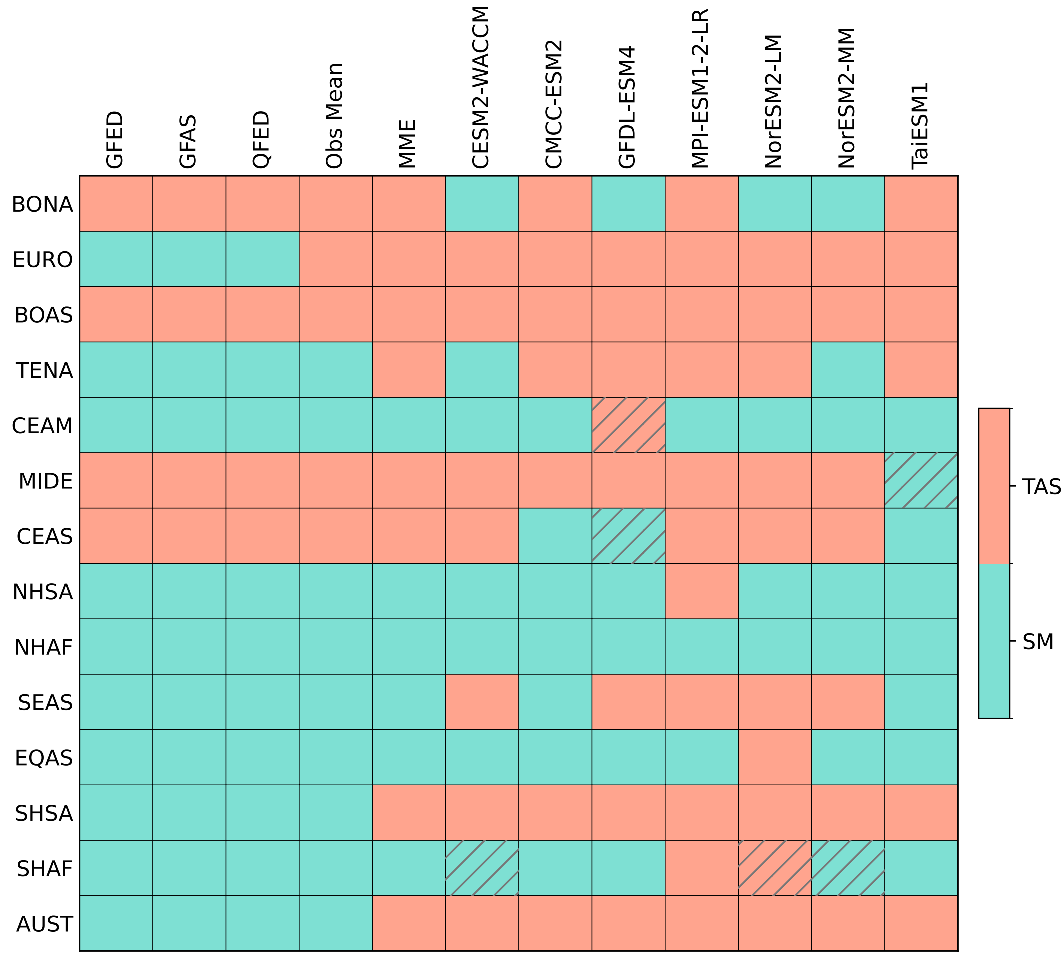

Fig. 7. Heatmap illustrating the relative greater importance of SM and TAS in influencing fire carbon emissions across the 14 GFED regions for individual CMIP6 models. The classification is based on standardized sensitivity coefficients. Pixels with diagonal hatching denote regions where the sensitivities are not statistically significant ($p > 0.05$).

the Amazon (0.03 PgC yr^{-2}, $p < 0.05$; Fig. S4 in the electronic supplementary material)—comparable in magnitude to the sum of NHSA and SHSA—largely accounts for the inflated tropical trend in the MME.

This model bias over the Amazon may stem from stronger-than-observed TAS levels and trends in many models (Figs. S1 and S5 in the electronic supplementary material), combined with elevated temperature sensitivity over SHSA (Figs. 6l and 7). In contrast, satellite-based products suggest that SM plays a more critical role in modulating emissions in SHSA. Despite a drying trend in SM (Fig. S6 in the electronic supplementary material), the relatively wet conditions over the Amazon in the observational datasets do not support high fire activity or upward trends (Figs. 2a and 9a–d, and Fig. S3 in the electronic supplementary material), highlighting the discrepancy in modeled versus observed fire–climate responses.

4. Discussion

Fire is one of the most significant natural disturbances affecting terrestrial ecosystems, and its impacts are intensifying under climate change. Over recent decades, an increasing number of CGCMs and ESMs have incorporated fire modules to better represent fire–climate–carbon interactions (Held et al., 2019; Walters et al., 2019; Zou et al., 2019; Danabasoglu et al., 2020). Large-scale intercomparison efforts, such as CMIP6 and FireMIP (Rabin et al., 2017), have substantially advanced global fire modeling and provided essential datasets for Earth system research. Despite these efforts, however, the magnitude and sources of inter-model uncertainties in reproducing historical fire activity remains insufficiently understood. Building on this foundation, earlier studies, such as Li et al. (2019, 2024), which evaluated global fire emissions and burned area in FireMIP and CMIP6, have identified major discrepancies in fire representation. More recently, Gallo et al. (2023) assessed burned areas across CMIP6 models and further highlighted substantial inter-model variability.

Our study delivers a comprehensive evaluation of present-day (2003–23) fire carbon emissions in CMIP6 models, with an emphasis on regional performance. Key aspects

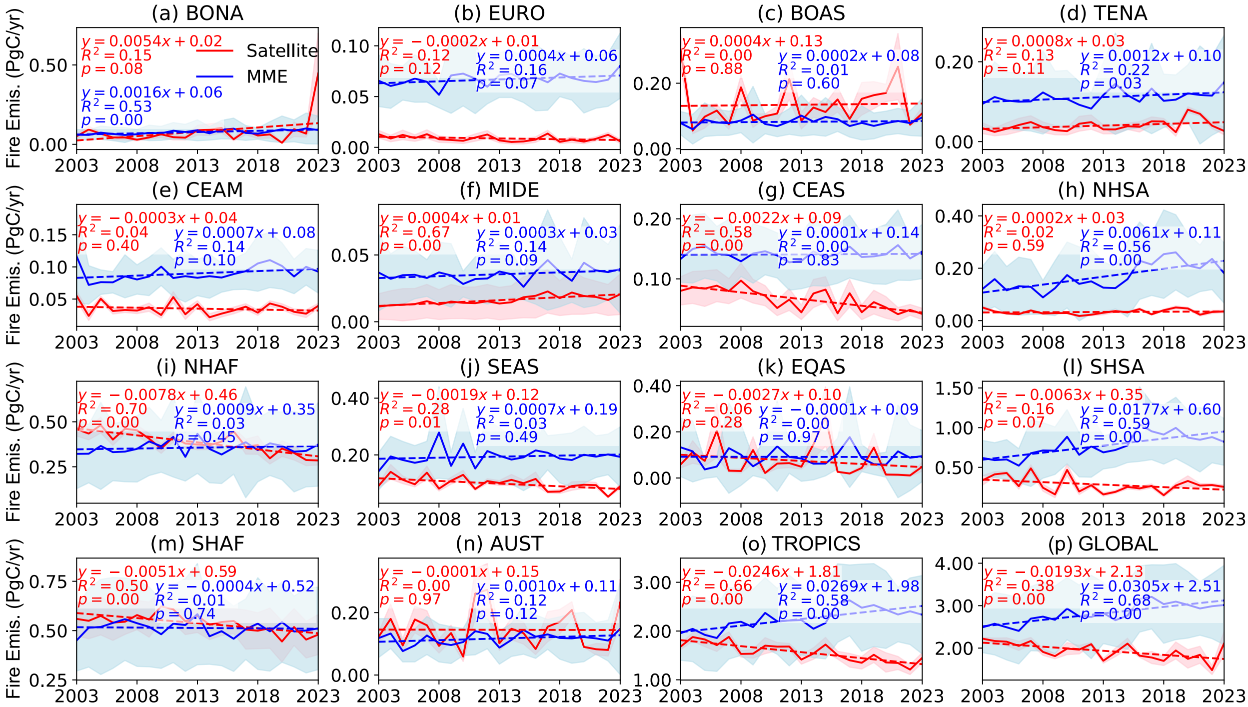

Fig. 8. Trends of annual fire carbon emissions from observational data and the CMIP6 MME across 14 regions, the tropics (30°S–30°N), and the globe. Red and blue solid lines represent the total emissions from the satellite-based products and MME during 2003–23, respectively. Red and blue dashed lines are their respective OLS (ordinary least squares) fitted trends. Pink and light blue shaded areas represent $\pm 1\sigma$ spread among individual members.

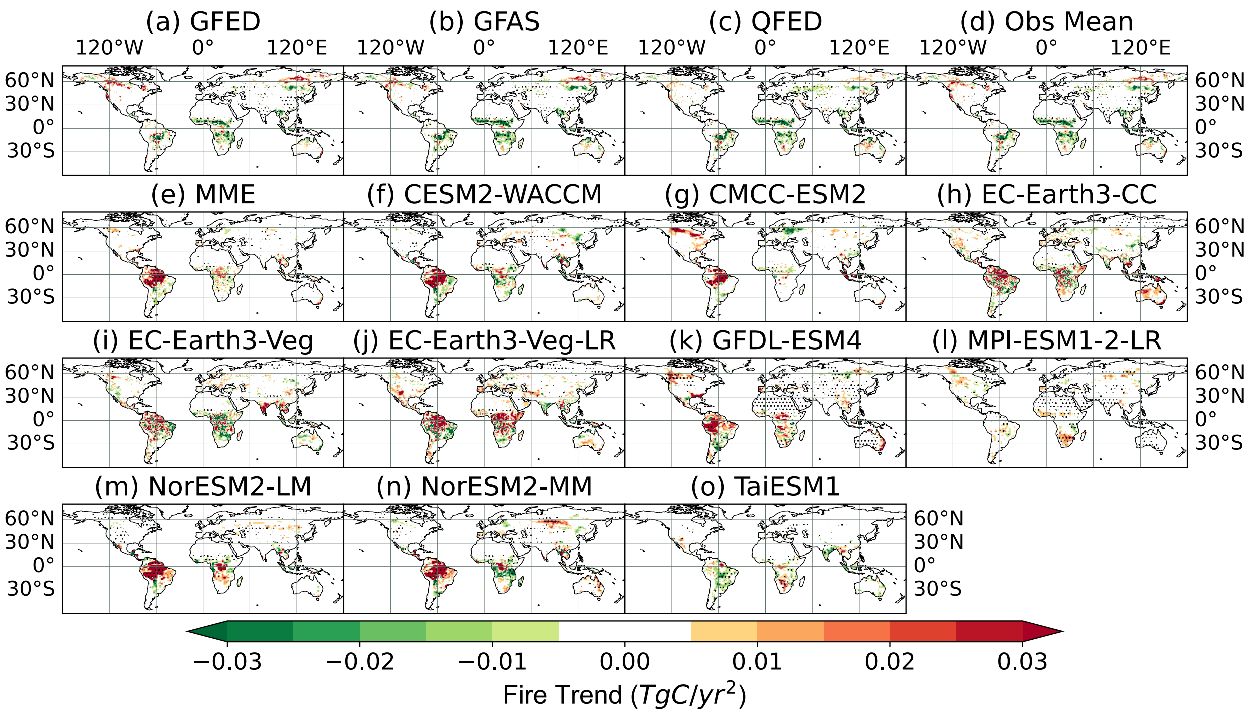

Fig. 9. Geographical distributions of fire carbon emission trends from 2003 to 2023 at 1° × 1° spatial resolution, based on observational data and CMIP6 model simulations. Red shading indicates positive trends, while blue indicates negative trends. Regions marked with symbols denote areas where the trends are statistically significant ($p < 0.05$).

include evaluations of climatological emissions, seasonal cycles, long-term trends, and—importantly—sensitivity to SM and TAS. In particular, we innovatively quantify the relative influence of SM and TAS on fire carbon emissions in each GFED region and across individual CMIP6 models. Our results aim to offer new insights and guidance for future model development and optimization.

It is well established that fire carbon emissions are governed by complex interactions among meteorological conditions, vegetation types, fuel availability, and human activities (Loehman, 2020; Wang et al., 2023; Kreider et al., 2024). Consequently, model biases in simulated fire emissions often stem from multiple sources, including uncertainties in fire parameterization schemes, meteorological inputs, and vegetation or fuel characteristics (Lasslop et al., 2014; Zou et al., 2019).

In our analysis, we note that the CMIP6 models adopt different fire schemes, each with distinct assumptions and parameterizations (Table 1). Five models (CESM-WACCM, CMCC-ESM2, GFDL-ESM4, NorESM2-LM, NorESM2-MM) implement the Li scheme or its modified versions (Li et al., 2012, 2013; Li and Lawrence, 2017; Ward et al., 2018), which refine agricultural fire dynamics and incorporate anthropogenic influences such as deforestation, human ignition, and suppression. Three EC-Earth3 variants use the GlobFIRM (Thonicke et al., 2001), while TaiESM1 applies a modified version of GlobFIRM (Kloster et al., 2010); these schemes do not explicitly account for human effects. MPI-ESM1-2-LR employs a modified SPITFIRE scheme (Lasslop et al., 2014), which considers both human ignition and suppression but assumes zero burned area and emissions over managed croplands. These differences in fire schemes can lead to substantial variability in model-simulated fire carbon emissions. Additionally, model resolution plays an important role—for instance, differences between NorESM2-LM and NorESM2-MM are evident over the semiarid SHAF and central Eurasia near 60°N (Figs. 9m, n).

Moreover, the reliability of fire simulations is further complicated by biases in model-simulated meteorological variables. Many studies have documented considerable uncertainties in CMIP6 surface meteorological elements due to the inaccurate representation of large-scale climate drivers and teleconnections (Kim et al., 2020; Rivera and Arnould, 2020; Turnock et al., 2020; Zhu and Yang, 2020; Tebaldi et al., 2021; Yang et al., 2021). These biases can propagate into fire simulations by misrepresenting key drivers such as temperature, precipitation, and humidity. Variations in fuel load—affected by aboveground biomass and plant functional types (PFTs)—are another critical source of uncertainty in estimating fire emissions (Brooks et al., 2004; Loudermilk et al., 2022). In this study, we did not delve deeply into the underlying causes related to meteorological or vegetation-related biases, as these have been examined in previous CMIP6 climate and carbon cycle studies (Kim et al., 2020; Hirsch et al., 2021; Li et al., 2021; Lauer et al., 2023). Instead, our sensitivity analysis focused solely on climatic drivers. We acknowledge, however, that fire carbon emissions are also influenced by vegetation, biomass, land use, and anthropogenic activities, and we plan to incorporate these additional factors in future work to provide a more comprehensive assessment of fire carbon emission sensitivities.

The large biases in simulated fire carbon emission trends across CMIP6 models raise serious concerns about our ability to assess future fire-related carbon risks with confidence. Satellite-based products consistently show significant declines in emissions over key tropical fire regions—such as the semi-arid zones of Africa, the Amazon margins, and Southeast Asia—yet most models fail to reproduce these trends, often projecting stable or increasing emissions. These discrepancies likely arise from insufficient representation of human activities, simplified fire–climate interactions, and differences in fire scheme implementation. Moreover, we note that even when models employ the same fire scheme, disparities in the trends of fire-induced carbon emissions persist. For instance, although all three models in the EC-Earth3 series use the identical GlobFIRM scheme, EC-Earth3-Veg-LR exhibits an opposing trend over Africa compared to the other two (Figs. 9h–j). Similarly, CESM2-WACCM and the two NorESM2 models—both utilizing the Li scheme in CLM5—also show divergent trends in the high-latitude Northern Hemisphere (Figs. 9f, m, n). These differences likely stem from uncertainties in other climatic or vegetation-related variables, making it challenging to determine which fire scheme performs best. These uncertainties are especially problematic in tropical ecosystems, where fire emissions are highly sensitive to both climatic variability and human-driven land-use change. As a result, improving fire modules and better integrating socio-environmental feedbacks are essential steps toward reducing uncertainty and supporting robust projections of fire-carbon dynamics under future climate scenarios.

5. Conclusion

This study comprehensively evaluates fire carbon emissions from 10 CMIP6 models and their MME across spatial, temporal, and climatic dimensions. While the models broadly capture the spatial pattern of fire emissions in tropical and high-latitude Northern Hemisphere regions, they exhibit substantial biases in magnitude, particularly over the Amazon, Africa, and the Indo-China Peninsula. Taylor diagrams highlight considerable inter-model spread in spatial correlation, normalized standard deviation, and centered RMSE.

Regionally, the MME performs well in only 5 out of 14 GFED regions, with prevalent overestimations across the tropics and in global totals. Seasonal cycles are generally reproduced within one month of observations, though notable biases persist, such as in BOAS where spring peaks are poorly captured. Sensitivity analyses reveal strong regional divergence: the MME reproduces TAS sensitivities at high latitudes but overestimates both TAS and SM responses in midlatitudes. In tropical and Southern Hemisphere extratropical regions, model performance degrades, with incorrect sign or magnitude of sensitivities—such as the reversed TAS response in SEAS and underestimated SM sensitivity in SHAF and EQAS.

Trend analysis from 2003 to 2023 shows observed increases in BONA and MIDE, alongside widespread declines in tropical regions (e.g., SHSA, NHAF, SHAF), contributing to an overall decrease in tropical and global fire emissions. In contrast, the MME captures only the BONA increase and fails to reproduce tropical declines, instead simulating spurious increases—particularly in SHSA and NHSA—leading to unrealistic rises in both tropical and global totals. These discrepancies are largely attributable to inadequate representation of anthropogenic fire suppression and overestimated temperature sensitivity in the models, especially across Southern Hemisphere fire-prone regions.

Acknowledgements. The calculations in this paper were carried out at the computing facilities in the High Performance Computing Center (HPCC) of Nanjing University. This study was supported by the National Natural Science Foundation of China (Grant No. 42475129) and the Natural Science Foundation of Jiangsu Province, China (Grant No. BK20221449). QZ was supported by the Taishan Scholar project (Grant No. tsqn202306210).

***Electronic supplementary material*:** Supplementary material is available in the online version of this article at https://doi.org/10.1007/s00376-025-5309-5.

***Data availability statement*.** CMIP6 outputs can be downloaded from Earth System Grid Federation (ESGF) at https://aims2.llnl.gov/search/cmip6/. The Global Fire Emission Database (GFED4s) results can be freely downloaded from https://www.geo.vu.nl/~gwerf/GFED/GFED4/. The Global Fire Assimilation System (GFASv1.2) can be downloaded from Copernicus Atmosphere Monitoring Service (CAMS) at https://ads.atmosphere.copernicus.eu/datasets/cams-global-fire-emissions-gfas?tab=download. The Quick Fire Emission Database (QFEDv2.6) can be downloaded from National Aeronautics and Space Administration (NASA) at https://portal.nccs.nasa.gov/datashare/iesa/aerosol/emissions/QFED/v2.6r1/.

REFERENCES

Abatzoglou, J. T., and A. P. Williams, 2016: Impact of anthropogenic climate change on wildfire across western US forests. *Proceedings of the National Academy of Sciences of the United States of America*, **113**, 11 770–11 775, https://doi.org/10.1073/pnas.1607171113.

Abram, N. J., and Coauthors, 2021: Connections of climate change and variability to large and extreme forest fires in southeast Australia. *Communications Earth & Environment*, **2**, 8, https://doi.org/10.1038/s43247-020-00065-8.

Andela, N., and Coauthors, 2017: A human-driven decline in global burned area. *Science*, **356**, 1356–1362, https://doi.org/10.1126/science.aal4108.

Andela, N., D. C. Morton, L. Giglio, R. Paugam, Y. Chen, S. Hantson, G. R. Van Der werf, and J. T. Randerson, 2019: The Global Fire Atlas of individual fire size, duration, speed and direction. *Earth System Science Data*, **11**, 529–552, https://doi.org/10.5194/essd-11-529-2019.

Archibald, S., and Coauthors, 2018: Biological and geophysical feedbacks with fire in the Earth system. *Environmental Research Letters*, **13**, 033003, https://doi.org/10.1088/1748-9326/aa9ead.

Bentsen, M., and Coauthors, 2019: NCC NorESM2-MM model output prepared for CMIP6 CMIP historical. Earth System Grid Federation. [Available online from https://www.wdc-climate.de/ui/cmip6?input=CMIP6.CMIP.NCC.NorESM2-MM.historical]

Brooks, M. L., and Coauthors, 2004: Effects of invasive alien plants on fire regimes. *Bioscience*, **54**, 677–688, https://doi.org/10.1641/0006-3568(2004)054[0677:Eoiapo]2.0.Co;2.

Byrne, B., and Coauthors, 2024: Carbon emissions from the 2023 Canadian wildfires. *Nature*, **633**, 835–839, https://doi.org/10.1038/s41586-024-07878-z.

Chuvieco, E., and Coauthors, 2019: Historical background and current developments for mapping burned area from satellite Earth observation. *Remote Sensing of Environment*, **225**, 45–64, https://doi.org/10.1016/j.rse.2019.02.013.

Danabasoglu, G., 2019: NCAR CESM2-WACCM model output prepared for CMIP6 ScenarioMIP. Earth System Grid Federation. [Available from https://www.wdc-climate.de/ui/cmip6?input=CMIP6.ScenarioMIP.NCAR.CESM2-WACCM]

Danabasoglu, G., and Coauthors, 2020: The Community Earth System Model Version 2 (CESM2). *Journal of Advances in Modeling Earth Systems*, **12**, e2019MS001916, https://doi.org/10.1029/2019MS001916.

EC-Earth Consortium, 2019: EC-Earth-Consortium EC-Earth3-Veg model output prepared for CMIP6 CMIP. Earth System Grid Federation. [Available online from https://www.wdc-climate.de/ui/cmip6?input=CMIP6.CMIP.EC-Earth-Consortium.EC-Earth3-Veg]

EC-Earth Consortium, 2020a: EC-Earth-Consortium EC-Earth-3-CC model output prepared for CMIP6 CMIP. Earth System Grid Federation. [Available online from https://www.wdc-climate.de/ui/cmip6?input=CMIP6.CMIP.EC-Earth-Consortium.EC-Earth3-CC]

EC-Earth Consortium, 2020b: EC-Earth-Consortium EC-Earth3-Veg-LR model output prepared for CMIP6 CMIP. Earth System Grid Federation. [Available online from https://www.wdc-climate.de/ui/cmip6?input=CMIP6.CMIP.EC-Earth-Consortium.EC-Earth3-Veg-LR]

Eyring, V., S. Bony, G. A. Meehl, C. A. Senior, B. Stevens, R. J. Stouffer, and K. E. Taylor, 2016: Overview of the Coupled Model Intercomparison Project Phase 6 (CMIP6) experimental design and organization. *Geoscientific Model Development*, **9**, 1937–1958, https://doi.org/10.5194/gmd-9-1937-2016.

Flannigan, M. D., M. A. Krawchuk, W. J. de Groot, B. M. Wotton, and L. M. Gowman, 2009: Implications of changing climate for global wildland fire. *International Journal of Wildland Fire*, **18**, 483–507, https://doi.org/10.1071/wf08187.

Gallo, C., J. M. Eden, B. Dieppois, I. Drobyshev, P. Z. Fulé, J. San-Miguel-Ayanz, and M. Blackett, 2023: Evaluation of CMIP6 model performances in simulating fire weather spatiotemporal variability on global and regional scales. *Geoscientific Model Development*, **16**, 3103–3122, https://doi.org/10.5194/gmd-16-3103-2023.

Giglio, L., J. T. Randerson, G. R. van der Werf, P. S. Kasibhatla, G. J. Collatz, D. C. Morton, and R. S. DeFries, 2010: Assessing variability and long-term trends in burned area by merging multiple satellite fire products. *Biogeosciences*, **7**, 1171–1186, https://doi.org/10.5194/bg-7-1171-2010.

Giglio, L., J. T. Randerson, and G. R. van der Werf, 2013: Analysis of daily, monthly, and annual burned area using the fourthgeneration global fire emissions database (GFED4). *J. Geophys. Res.*, **118**, 317–328, https://doi.org/10.1002/jgrg.20042.

Gleckler, P. J., K. E. Taylor, and C. Doutriaux, 2008: Performance metrics for climate models. *J. Geophys. Res.*, **113**, D06104, https://doi.org/10.1029/2007JD008972.

Grégoire, J. M., K. Tansey, and J. M. N. Silva, 2003: The GBA2000 initiative: Developing a global burnt area database from SPOT-VEGETATION imagery. *Int. J. Remote Sens.*, **24**, 1369–1376, https://doi.org/10.1080/0143116021000044850.

Hantson, S., and Coauthors, 2016: The status and challenge of global fire modelling. *Biogeosciences*, **13**, 3359–3375, https://doi.org/10.5194/bg-13-3359-2016.

He, J. Y., D. Chen, L. Jenkins, and T. V. Loboda, 2021: Impacts of wildfire and landscape factors on organic soil properties in Arctic tussock tundra. *Environmental Research Letters*, **16**, 085004, https://doi.org/10.1088/1748-9326/ac1192.

Held, I. M., and Coauthors, 2019: Structure and performance of GFDL's CM4.0 climate model. *Journal of Advances in Modeling Earth Systems*, **11**, 3691–3727, https://doi.org/10.1029/2019ms001829.

Hirsch, A. L., N. N. Ridder, S. E. Perkins-Kirkpatrick, and A. Ukkola, 2021: CMIP6 MultiModel evaluation of present-day heatwave attributes. *Geophys. Res. Lett.*, **48**, e2021GL095161, https://doi.org/10.1029/2021GL095161.

Jones, M. W., and Coauthors, 2022: Global and regional trends and drivers of fire under climate change. *Rev. Geophys.*, **60**, e2020RG000726, https://doi.org/10.1029/2020RG000726.

Jones, P. W., 1999: First- and second-order conservative remapping schemes for grids in spherical coordinates. *Mon. Wea. Rev.*, **127**, 2204–2210, https://doi.org/10.1175/1520-0493(1999)127<2204:Fasocr>2.0.Co;2.

Kaiser, J. W., and Coauthors, 2012: Biomass burning emissions estimated with a global fire assimilation system based on observed fire radiative power. *Biogeosciences*, **9**, 527–554, https://doi.org/10.5194/bg-9-527-2012.

Kim, Y.-H., S.-K. Min, X. B. Zhang, J. Sillmann, and M. Sandstad, 2020: Evaluation of the CMIP6 multi-model ensemble for climate extreme indices. *Weather and Climate Extremes*, **29**, 100269, https://doi.org/10.1016/j.wace.2020.100269.

Kloster, S., and Coauthors, 2010: Fire dynamics during the 20th century simulated by the Community Land Model. *Biogeosciences*, **7**, 1877–1902, https://doi.org/10.5194/bg-7-1877-2010.

Koster, R. D., A. S. Darmenov, and A. M. da Silva, 2015: The Quick Fire Emissions Dataset (QFED): Documentation of versions 2.1, 2.2 and 2.4. Vol. 38, Technical Report Series on Global Modeling and Data Assimilation, NASA/TM-2015-104606.

Krasting, J. P., and Coauthors, 2018: NOAA-GFDL GFDL-ESM4 model output prepared for CMIP6 CMIP. Earth System Grid Federation. Available from https://www.wdc-climate.de/ui/cmip6?input=CMIP6.CMIP.NOAA-GFDL.GFDL-ESM4.

Kreider, M. R., P. E. Higuera, S. A. Parks, W. L. Rice, N. White, and A. J. Larson, 2024: Fire suppression makes wildfires more severe and accentuates impacts of climate change and fuel accumulation. *Nature Communications*, **15**, 2412, https://doi.org/10.1038/s41467-024-46702-0.

Larjavaara, M., J. Pennanen, and T. J. Tuomi, 2005: Lightning that ignites forest fires in Finland. *Agricultural and Forest Meteorology*, **132**, 171–180, https://doi.org/10.1016/j.agrformet.2005.07.005.

Lasslop, G., K. Thonicke, and S. Kloster, 2014: SPITFIRE within the MPI Earth system model: Model development and evaluation. *Journal of Advances in Modeling Earth Systems*, **6**, 740–755, https://doi.org/10.1002/2013MS000284.

Lasslop, G., A. I. Coppola, A. Voulgarakis, C. Yue, and S. Veraverbeke, 2019: Influence of fire on the carbon cycle and climate. *Current Climate Change Reports*, **5**, 112–123, https://doi.org/10.1007/s40641-019-00128-9.

Lauer, A., L. Bock, B. Hassler, M. Schröder, and M. Stengel, 2023: Cloud climatologies from global climate models-a comparison of CMIP5 and CMIP6 models with satellite data. *J. Climate*, **36**, 281–311, https://doi.org/10.1175/Jcli-D-22-0181.1.

Lee, W.-L., and H.-C. Liang, 2023: IPCC DDC: AS-RCEC TaiESM1.0 model output prepared for CMIP6 CMIP. Earth System Grid Federation. [Available online from https://b2find.eudat.eu/dataset/81901885-662f-5dd3-a9d4-c668b1e47a09]

Li, F., and D. M. Lawrence, 2017: Role of fire in the global land water budget during the twentieth century due to changing ecosystems. *J. Climate*, **30**, 1893–1908, https://doi.org/10.1175/Jcli-D-16-0460.1.

Li, F., X. D. Zeng, and S. Levis, 2012: A process-based fire parameterization of intermediate complexity in a Dynamic Global Vegetation Model. *Biogeosciences*, **9**, 2761–2780, https://doi.org/10.5194/bg-9-2761-2012.

Li, F., S. Levis, and D. S. Ward, 2013: Quantifying the role of fire in the Earth system–Part 1: Improved global fire modeling in the Community Earth System Model (CESM1). *Biogeosciences*, **10**, 2293–2314, https://doi.org/10.5194/bg-10-2293-2013.

Li, F., and Coauthors, 2019: Historical (1700–2012) global multi-model estimates of the fire emissions from the Fire Modeling Intercomparison Project (FireMIP). *Atmospheric Chemistry and Physics*, **19**, 12 545–12 567, https://doi.org/10.5194/acp-19-12545-2019.

Li, F., and Coauthors, 2024: Evaluation of global fire simulations in CMIP6 Earth system models. *Geoscientific Model Development*, **17**, 8751–8771, https://doi.org/10.5194/gmd-17-8751-2024.

Li, J. D., C. Y. Miao, W. Wei, G. Zhang, L. J. Hua, Y. L. Chen, and X. X. Wang, 2021: Evaluation of CMIP6 global climate models for simulating land surface energy and water fluxes during 1979–2014. *Journal of Advances in Modeling Earth Systems*, **13**, e2021MS002515, https://doi.org/10.1029/2021MS002515.

Liu, Z. W., J. M. Eden, B. Dieppois, and M. Blackett, 2022: A global view of observed changes in fire weather extremes: Uncertainties and attribution to climate change. *Climatic Change*, **173**, 14, https://doi.org/10.1007/s10584-022-03409-9.

Loehman, R. A., 2020: Drivers of wildfire carbon emissions. *Nature Climate Change*, **10**, 1070–1071, https://doi.org/10.1038/s41558-020-00922-6.

Loudermilk, E. L., J. J. O'Brien, S. L. Goodrick, R. R. Linn, N. S. Skowronski, and J. K. Hiers, 2022: Vegetation's influence on fire behavior goes beyond just being fuel. *Fire Ecology*, **18**, 9, https://doi.org/10.1186/s42408-022-00132-9.

Lovato, T., D. Peano, and M. Butenschön, 2021: CMCC CMCC-ESM2 model output prepared for CMIP6 CMIP. Earth System Grid Federation. [Available online from https://www.wdc-climate.de/ui/cmip6?input=CMIP6.CMIP.CMCC.CMCC-ESM2]

Luo, K. W., X. L. Wang, M. de Jong, and M. Flannigan, 2024: Drought triggers and sustains overnight fires in North America. *Nature*, **627**, 321–327, https://doi.org/10.1038/s41586-024-07028-5.

Martínez, J., C. Vega-Garcia, and E. Chuvieco, 2009: Human-caused wildfire risk rating for prevention planning in Spain. *Journal of Environmental Management*, **90**, 1241–1252, https://doi.org/10.1016/j.jenvman.2008.07.005.

Muñoz-Sabater, J., and Coauthors, 2021: ERA5-Land: a state-of-the-art global reanalysis dataset for land applications. *Earth System Science Data*, **13**, 4349–4383, https://doi.org/10.5194/essd-13-4349-2021.

Padilla, M., and C. Vega-García, 2011: On the comparative importance of fire danger rating indices and their integration with spatial and temporal variables for predicting daily human-caused fire occurrences in Spain. *International Journal of Wildland Fire*, **20**, 46–58, https://doi.org/10.1071/Wf09139.

Rabin, S. S., and Coauthors, 2017: The Fire Modeling Intercomparison Project (FireMIP), phase 1: Experimental and analytical protocols with detailed model descriptions. *Geoscientific Model Development*, **10**, 1175–1197, https://doi.org/10.5194/gmd-10-1175-2017.

Radeloff, V. C., R. B. Hammer, S. I. Stewart, J. S. Fried, S. S. Holcomb, and J. F. McKeefry, 2005: The wildland–urban interface in the united states. *Ecological Applications*, **15**, 799–805, https://doi.org/10.1890/04-1413.

Ramo, R., E. Roteta, I. Bistinas, D. van Wees, A. Bastarrika, E. Chuvieco, and G. R. van der Werf, 2021: African burned area and fire carbon emissions are strongly impacted by small fires undetected by coarse resolution satellite data. *Proceedings of the National Academy of Sciences of the United States of America*, **118**, e2011160118, https://doi.org/10.1073/pnas.2011160118.

Rivera, J. A., and G. Arnould, 2020: Evaluation of the ability of CMIP6 models to simulate precipitation over Southwestern South America: Climatic features and long-term trends (1901–2014). *Atmospheric Research*, **241**, 104953, https://doi.org/10.1016/j.atmosres.2020.104953.

Scholze, M., and Coauthors, 2012: Earth system models: A tool to understand changes in the Earth system. *Understanding the Earth System: Global Change Science for Application*, S. E. Cornell, I. C. Prentice, J. I. House, and C. J. Downy, Eds., Cambridge University Press, 129–159. https://doi.org/10.1017/CBO9780511921155.008.

Seiler, W., and P. J. Crutzen, 1980: Estimates of gross and net fluxes of carbon between the biosphere and the atmosphere from biomass burning. *Climatic Change*, **2**, 207–247, https://doi.org/10.1007/BF00137988.

Seland, Ø., and Coauthors, 2019: NCC NorESM2-LM model output prepared for CMIP6 CMIP. Earth System Grid Federation. Earth System Grid Federation. [Available online from https://www.wdc-climate.de/ui/cmip6?input=CMIP6.CMIP.NCC.NorESM2-LM.historical]

Simon, M., S. Plummer, F. Fierens, J. J. Hoelzemann, and O. Arino, 2004: Burnt area detection at global scale using ATSR-2: The GLOBSCAR products and their qualification. *J. Geophys. Res.*, **109**, D14S02, https://doi.org/10.1029/2003JD003622.

Sommers, W. T., R. A. Loehman, and C. C. Hardy, 2014: Wildland fire emissions, carbon, and climate: Science overview and knowledge needs. *Forest Ecology and Management*, **317**, 1–8, https://doi.org/10.1016/j.foreco.2013.12.014.

Taylor, K. E., 2001: Summarizing multiple aspects of model performance in a single diagram. *J. Geophys. Res.*, **106**, 7183–7192, https://doi.org/10.1029/2000jd900719.

Tebaldi, C., and Coauthors, 2021: Climate model projections from the Scenario Model Intercomparison Project (ScenarioMIP) of CMIP6. *Earth System Dynamics*, **12**, 253–293, https://doi.org/10.5194/esd-12-253-2021.

Thonicke, K., S. Venevsky, S. Sitch, and W. Cramer, 2001: The role of fire disturbance for global vegetation dynamics: Coupling fire into a Dynamic Global Vegetation Model. *Global Ecology and Biogeography*, **10**, 661–677, https://doi.org/10.1046/j.1466-822X.2001.00175.x.

Turnock, S. T., and Coauthors, 2020: Historical and future changes in air pollutants from CMIP6 models. *Atmospheric Chemistry and Physics*, **20**, 14 547–14 579, https://doi.org/10.5194/acp-20-14547-2020.

van der Werf, G. R., and Coauthors, 2017: Global fire emissions estimates during 1997–2016. *Earth System Science Data*, **9**, 697–720, https://doi.org/10.5194/essd-9-697-2017.

van Marle, M. J. E., and Coauthors, 2017: Historic global biomass burning emissions for CMIP6 (BB4CMIP) based on merging satellite observations with proxies and fire models (1750–2015). *Geoscientific Model Development*, **10**, 3329–3357, https://doi.org/10.5194/gmd-10-3329-2017.

Verdú, F., J. Salas, and C. Vega-García, 2012: A multivariate analysis of biophysical factors and forest fires in Spain, 1991–2005. *International Journal of Wildland Fire*, **21**, 498–509, https://doi.org/10.1071/WF11100.

Walters, D., and Coauthors, 2019: The Met Office Unified Model Global Atmosphere 7.0/7.1 and JULES Global Land 7.0 configurations. *Geoscientific Model Development*, **12**, 1909–1963, https://doi.org/10.5194/gmd-12-1909-2019.

Wang, J., Z. Q. Liu, N. Zeng, F. Jiang, H. M. Wang, and W. M. Ju, 2020: Spaceborne detection of XCO_2 enhancement induced by Australian mega-bushfires. *Environmental Research Letters*, **15**, 124069, https://doi.org/10.1088/1748-9326/abc846.

Wang, S. S. C., L. R. Leung, and Y. Qian, 2023: Extension of large fire emissions from summer to autumn and its drivers in the western US. *Earth's Future*, **11**, e2022EF003086, https://doi.org/10.1029/2022EF003086.

Ward, D. S., E. Shevliakova, S. Malyshev, and S. Rabin, 2018: Trends and variability of global fire emissions due to historical anthropogenic activities. *Global Biogeochemical Cycles*, **32**, 122–142, https://doi.org/10.1002/2017gb005787.

Westerling, A. L., H. G. Hidalgo, D. R. Cayan, and T. W. Swetnam, 2006: Warming and earlier spring increase western U.S. forest wildfire activity. *Science*, **313**, 940–943, https://doi.org/10.1126/science.1128834.

Wieners, K.-H., and Coauthors, 2019: MPI-M MPIESM1.2-LR model output prepared for CMIP6 CMIP. Earth System Grid Federation. Earth System Grid Federation. Available from https://www.wdc-climate.de/ui/cmip6?input=CMIP6.CMIP.MPI-M.MPI-ESM1-2-LR.

Yang, X. L., B. T. Zhou, Y. Xu, and Z. Y. Han, 2021: CMIP6 evaluation and projection of temperature and precipitation over China. *Adv. Atmos. Sci.*, **38**, 817−830, https://doi.org/10.1007/s00376-021-0351-4.

Zheng, B., and Coauthors, 2023: Record-high CO_2 emissions from boreal fires in 2021. *Science*, **379**, 912−917, https://doi.org/10.1126/science.ade0805.

Zhu, Y.-Y., and S. N. Yang, 2020: Evaluation of CMIP6 for historical temperature and precipitation over the Tibetan Plateau and its comparison with CMIP5. *Advances in Climate Change Research*, **11**, 239−251, https://doi.org/10.1016/j.accre.2020.08.001.

Zou, Y. F., Y. H. Wang, Z. M. Ke, H. Q. Tian, J. Yang, and Y. Q. Liu, 2019: Development of a REgion-specific ecosystem feedback fire (RESFire) model in the community earth system model. *Journal of Advances in Modeling Earth Systems*, **11**, 417−445, https://doi.org/10.1029/2018ms001368.